Check for updates

The role of internal architecture in producing high-strength 3D printed cobalt-chromium objects

Abdullah Jasim Mohammed*, Ahmed Asim Al-Ali

Department of Prosthodontics, College of Dentistry, Mosul University, Mosul, Iraq

ORCID
Abdullah Jasim Mohammed
https://orcid.org/0000-0002-1466-513X

Ahmed Asim Al-Ali
https://orcid.org/0000-0003-2129-9622

PURPOSE. The objectives of the current study were to estimate the influence of self-reinforced hollow structures with a graded density on the dimensional accuracy, weight, and mechanical properties of Co-Cr objects printed with the direct metal laser sintering (DMLS) technique. **MATERIALS AND METHODS.** Sixty-five dog-bone samples were manufactured to evaluate the dimensional accuracy of printing, weight, and tensile properties of DMLS printed Co-Cr. They were divided into Group 1 (control) (n = 5), Group 2, 3, and 4 with incorporated hollow structures based on (spherical, elliptical, and diamond) shapes; they were subdivided into subgroups (n = 5) according to the volumetric reduction (10%, 15%, 20% and 25%). Radiographic imaging and microscopic analysis of the fractographs were conducted to validate the created geometries; the dimensional accuracy, weight, yield tensile strength, and modulus of elasticity were calculated. The data were estimated by one-way ANOVA and Duncan's tests at $P < .05$. **RESULTS.** The accuracy test showed an insignificant difference in the x, y, z directions in all printed groups. The weight was significantly reduced proportionally to the reduced volume fraction. The yield strength and elastic modulus of the control group and Group 2 at 10% volume reduction were comparable and significantly higher than the other subgroups. **CONCLUSION.** The printing accuracy was not affected by the presence or type of the hollow geometry. The weight of Group 2 at 10% reduction was significantly lower than that of the control group. The yield strength and elastic modulus of the Group 2 at a 10% reduction showed means equivalent to the compact objects and were significantly higher than other subgroups. [J Adv Prosthodont 2024;16:91-104]

KEYWORDS

Three-dimensional printing; CAD-CAM; Trueness; Denture design; Manufactured materials

Corresponding author
Abdullah Jasim Mohammed
Department of Prosthodontics,
College of Dentistry, Mosul
University, Al-Majmoa'a Street,
Mosul, 41002, Iraq
Tel +9647708234048
**E-mail**
AbdoAlla2009@uomosul.edu.iq

INTRODUCTION

Three dimensional printing's unique capabilities have driven recent interest in additive manufacturing (AM) to generate predetermined intricate geometries. AM processes add layers of material successively to build a complex object. Compared to conventional techniques, additive manufacturing provides great freedom from geometrical limitations and can conveniently produce components that are difficult or impossible to produce using traditional methods.[1,2] Due to a condensed manufacturing cycle of operation, a component with an intricate geometric form can be manufactured in a short amount of time, simultaneously with the development of additive manufacturing techniques (for instance, the lattice designs with a higher degree of architectural freedom, including various minute, intricate geometrical details) can be created.[3-5] A typical scenario of an optimal topology is a strategy that reduces the structure's weight while meeting all physical and mechanical performance requirements.[6,7] Previous studies demonstrated higher energy absorption by integrating topologically optimized structures in solid objects.[8,9] For the fabrication of hollow structures, 3D printing techniques are evolving and becoming feasible. The selective laser melting (SLM) is recognized for its production independence among the most promising additive manufacturing technologies.[10,11] The samples printed with the SLM have exceptional mechanical properties and can produce 3D printed metal with variable density levels.[12] The laser performs selective particle layer melting based on the computer-aided design (CAD) Standard tesselation language (STL) file's specified shape. Each component layer is constructed in two phases using SLM. First, the perimeter is constructed, a process known as contouring, and then the material within the contour is fused to form one layer. This method is repeated until the desired three-dimensional component is complete.[13,14] Huang *et al*.[15] investigated the influence of topology optimization and printing parameters on the cost; they discovered that the cost was significantly reduced due to the weight reduction technique in topology optimization. Galeta *et al*.[16] evaluated honeycomb and lattice interior configurations with compact manufactured pieces. They asserted that the samples with honeycomb voids demonstrated superior tensile performance to that of the lattice form but inferior to that of the compacted specimens. Nonetheless, both designs showed sufficient tensile strength to be used as medical implants. Challis *et al*.[17] designed two-phase isotropic three-dimensional recurring substances with the highest modulus of bulk and conductance using topology optimization to enhance the microstructure of lattice solids with unique topological boundaries. Lesueur *et al*.[18] evaluated the impact of integrating macro-scale interior geometric shapes on the yield strength of the polylactic (PLA) printed items. They determined that the yield strength depended on the topological voids rather than the material used. However, no studies are available that evaluate the improvement of the yield strength at a comparable level with the compact objects without compromising the elastic modulus and printing dimensional accuracy of the direct metal laser sintering (DMLS) printed Co-Cr by incorporating novel custom-designed hollow structures implemented in the current study. For this reason, the current study aimed to estimate the influence of self-reinforced micro-voids as hollow structures with a graded density on the dimensional accuracy in the x, y, z directions, weight, the yield tensile strength, and elastic modulus (Young's modulus) of Co-Cr printed with DMLS technique. The study hypothesis was that the incorporation of multiple shapes and density graded self-reinforced hollow structures could improve the yield tensile strength of the topologically modified 3D printed Co-Cr without compromising the dimensional accuracy and the elastic modulus of the printed Co-Cr metal.

MATERIALS AND METHODS

Sixty-five dog-bone samples were fabricated per (ISO 22674:2016) with (15 mm working length, 4 mm width, and 1 mm thickness); the length of the sample (working length 15 mm + free length between the grip on each side and the working bar 3 mm + the length of each grip 6 mm) was (15 + (3 × 2) + (6 × 2) = 33 mm).[19] The dimensions and shape of the dog-bone specimen are illustrated in Fig. 1. The samples were created virtually by AutoCAD 2021 software program
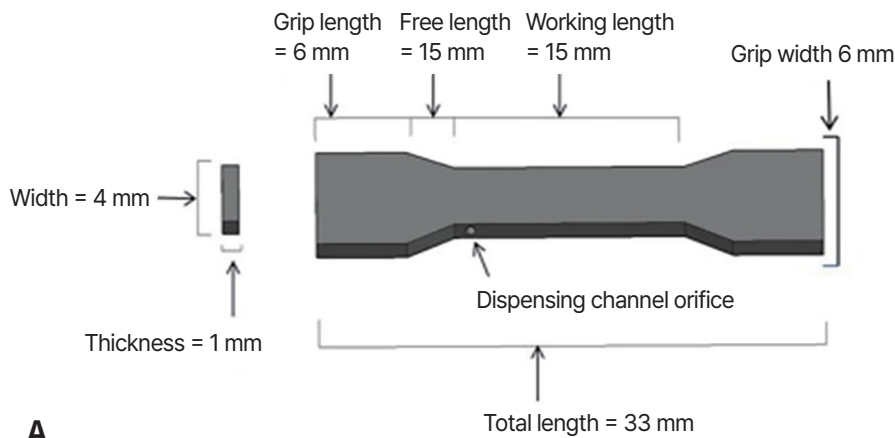
Fig. 1. Dog-bone shaped tensile test sample. (A) Diagram of the shape and dimensions of the dog-bone sample. (B) DMLS printed tensile test sample.

(AutoDesk Co., San Francisco, CA, USA) to integrate a self-reinforced custom-designed hollow structures in the core of the test samples. The virtual samples were prepared for 3D printing using Materialise Magics 2022 (Materialise Magics Co., Leuven, Belgium) as a slicer program. For this purpose, a powdered Co-Cr alloy was used to fabricate the samples (Adentatec, GmbH, Köln, Germany) and fabricated using a direct metal laser sintering (DMLS) machine (Riton, dual-150, Guangdong, China).

The samples were printed transversally at (0°), with fabrication parameters listed in (Table 1). The created samples were divided into four groups. The first group (Group 1) (n = 5) was compact, devoid of any internal hollow structure to be the control group, and Group 2 (n = 20) had a sphere-based hollow structure. Group 3 (n = 20) was fabricated with an ellipse-based hollow structure. Group 4 (n = 20) was fabricated with a diamond-based hollow structure. Each of the Group 2, 3, and 4 was subdivided into four subgroups according to the reduction percentage per volume (10%, 15%, 20%, and 25%) to render each final subgroup (n = 5) according to ASTM standard E9 (2000).[20]

The incorporated hollow structures were integrated as an enclosed cell configuration with a channel extended to the end of the sample to dispense the non-sintered alloy particles after the printing pro-

cess. Then, the dispensing channel's orifice was weld-plugged using Kobalt-Chrom-lot solder (Bego Co., Bremen, Germany) to preserve the constraint condition of the hollow structure (basic hollow geometries and the cylindrical connectors).[21] The soldering process started with grinding about 1 - 1.5 mm of the area around the dispensing channel orifice with aluminum oxide sandpaper; the samples then were invested with Biosint-supra phosphate bonded invest-

Table 1. Standard parameters of 3D printing process with Riton dual 150 machine

Parameter	Value
Laser speed	1050 mm/s
Laser power	165 W
Support laser power	140 W
Layer thickness (powder supply)	0.05 mm
Oxygen content	0.06%
Building plate	150 × 150 × 110 mm
Building direction	0 degree
Protect gas	Argon
Scan speed	14000 mm/s
Operating system	Windows XP
Wavelength	1064 µm

ment (Degussa Co., Frankfort, Germany) except for the area to be weld-plugged. The intended area was preheated for one minute according to the manufacturer's instructions; when the orifice area became dull red-colored, the soldering material was allowed to melt and fill the orifice area of the dispensing channel, and then the welded area was finished with sandpaper and rubber disk.

In Group 1, the samples had no internal geometries and were the constructed compact object (control group). In Group 2, the integrated structure was spherical-based following the topologic structure of Mackenzie,[22] with modifications where the spheres created ranged from 200 - 500 μm in diameter depending on the reduction percentage of volume, and they were connected with cylinders that had diameters of ≈50 - 75% of the diameter of the spherical shaped object; also, the length of the cylindrical tunnels among the spheres ranged from ≈50 - 125% to the diameter of the sphere according to the reduced volume percentage. In Group 3, an elliptical-base hollow structure was created, with ellipses aligned transversely with 200 - 500 μm lesser diameter. Cylindrical hollow connectors were used to connect the basic elliptical shapes using the same ratios of length and diameter according to the lesser diameter of the ellipses. The basic shape in the Group 4 was a diamond-based hollow structure. The diamond-based hollow structure was designed with a ratio of 1 : 1.5 horizontal to vertical diameters of 200 - 500 μm lesser diameter to ensure printability of the shape, and the connecting cylindrical hollow tunnels connected them with the same dimensions ratio using the horizontal diameter as a reference dimension. The diameter and length of the cylinder varied according to the percentage of the reduced volume. In all the virtual samples designed, the designed interior hollow structures were positioned at one level in the inner core of the sample. Each specimen's four lateral surfaces measured at least 0.5 mm in thickness. According to the reduction percentage, the upper and lower surfaces had a thickness range of 0.2 - 0.5 mm. The hollow structures of Group 2, 3, and 4 are shown in Fig. 2.

The dimensional accuracy was evaluated on the length, width, and thickness levels using an electronic digital caliper (S.H, Shanghai Shenhan Co.,

Shanghai, China) with 0 - 150 mm gauge and 0.00 mm precision. Then, the fabricated specimens were radiographed with a digital X-ray to verify the validity of the 3D printing of the specimens and the quality and extension of the soldering process using a digital dental radiographic machine (Planmeca, Helsinki, Finland). The quality of the printed hollow structures and the soldered orifice that was encircled with red were shown in the radiographic images in Fig. 3.

Then, the mass of the samples was measured using a digital balance (Mettler Toledo Ltd., Greifensee, Switzerland) with a precision of 0.000 g (PG 503-S MonoBloc inside, Mettler Toledo Ltd, Greifensee, Switzerland) to determine the reduction per mass of the samples.

The tensile test specimens were used as built without finishing and polishing procedures. The tensile test was conducted in an ambient atmosphere with a crosshead speed of 2 mm/min according to ISO 22674:2016.[19] The tensile test was conducted using a digital universal tensile testing machine (GESTER International Co., LTD, Fujian, China). The digitally drawn plot curve was used, as shown in Fig. 4, to calculate the yield tensile strength at 0.2% strain offset,[19,23,24] according to the following equation:[25]

$$\text{the yield tensile strength} = F / S_o$$

where F is the applied force at the yield point at 0.2% proof stress in the plot curve, S_o is the cross-sectional area of the sample.

The Young's modulus was calculated from the tensile stress/strain curve as shown in Fig. 4 according to the following equation:[19]

$$\text{elastic modulus (Young's modulus)} = \Delta F / S_o \times L_o / \Delta L$$

where F is the applied force, S_o is the cross-sectional area of the sample, L_o is the original working distance (length), and ΔL is the difference in length of the sample at the determined force points, as illustrated in Fig. 4.

To evaluate the changes in the hollow structures after the tensile stress application, the samples were cut to create cross sections with hollow shapes other than the fractographs, using a carbide disk (0.3 mm) and treated with sandpaper at a specific point located by a distance measured from the CAD designs. The fractographs of the tensile test specimens were
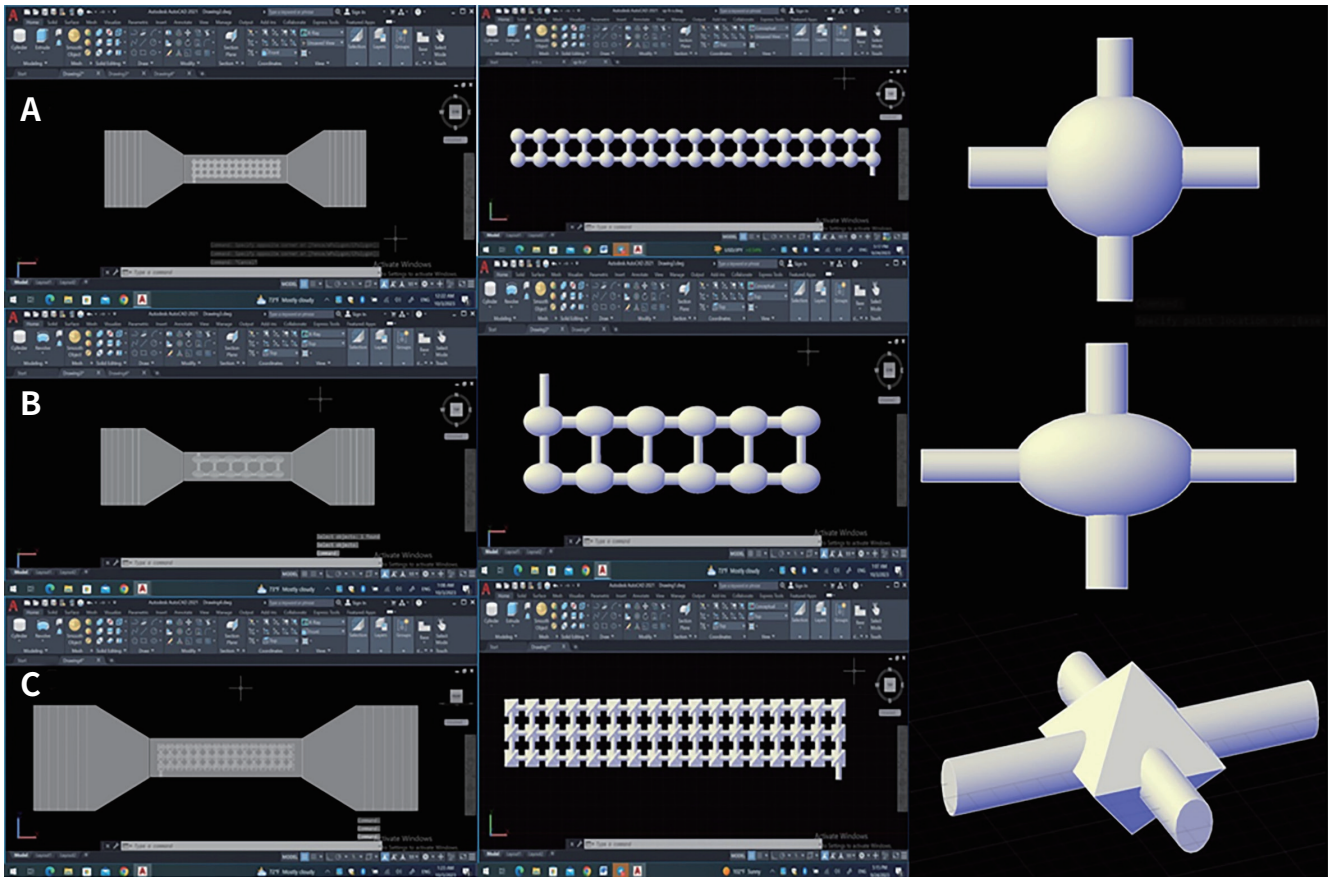
Fig. 2. Designs of the three types of architected hollow structures. Designed hollow structures. (A) Tensile test sample incorporated with sphere-based hollow structure with the isolated sphere-based hollow structure and the single unit of the hollow geometry. (B) Tensile test sample incorporated with ellipse-based hollow structure with the isolated ellipse-based hollow structure and the single unit of the hollow geometry. (C) Tensile test sample incorporated with diamond-based hollow structure with the isolated diamond-based hollow structure and the single unit of the hollow geometry.
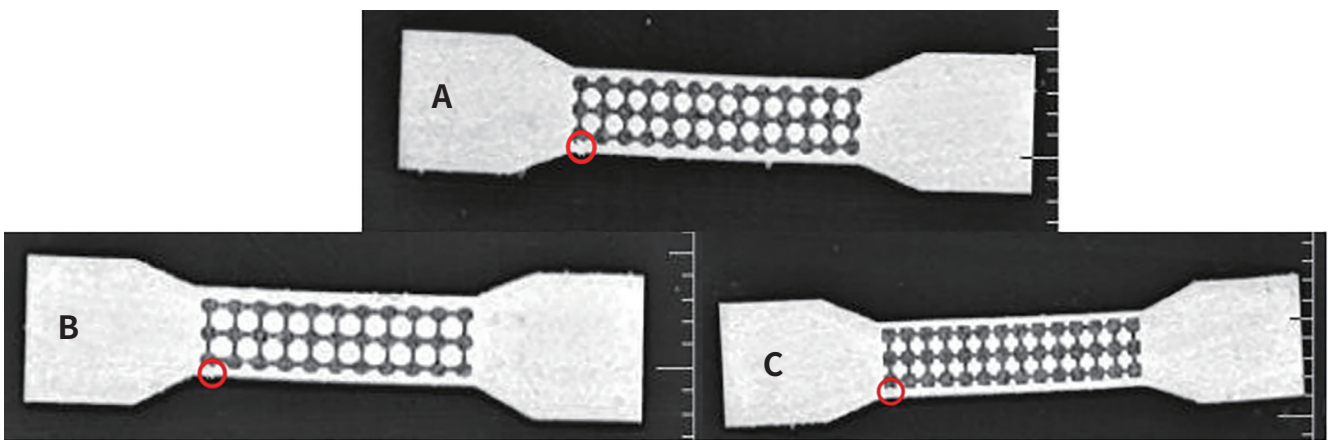
Fig. 3. Radiographic images of the samples with three incorporated geometries, with red circles to identify the end-welded orifices. (A) Tensile test sample with a sphere-based hollow structure. (B) Tensile test sample with an ellipse-based hollow structure. (C) Tensile test sample with a diamond-based hollow structure.
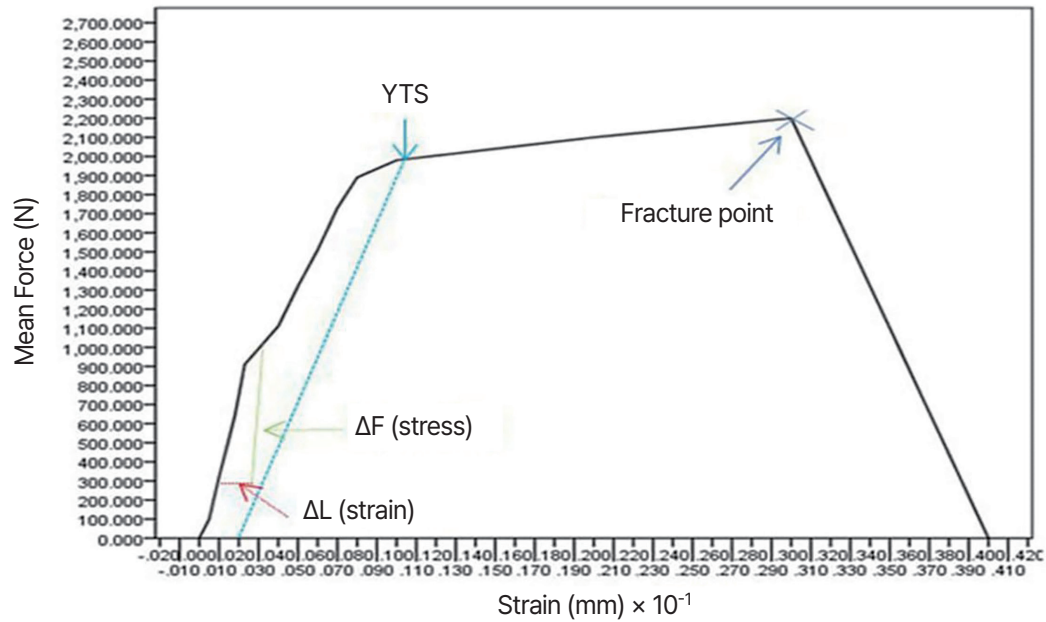
Fig. 4. Stress/strain curve where YTS is the yield tensile strength, the green line is the change in the applied force ΔF, and the red line is the change in length ΔL.

treated with sandpaper only and inspected by a material optical microscope (SLX, Optika Co., Bergamo, Italy) with magnification power of 4.5× to verify the production of hollow geometries and to estimate the crack propagation at the fracture site.

The statistical analyses were conducted by the SPSS 17 program (SPSS Inc., Chicago, IL, USA). ANOVA test and Duncan's post hoc test were conducted to estimate the statistical difference in means of the dimensional accuracy (width, length, and thickness), the weight, the yield tensile strength (YTS), and the elastic modulus at a significance level of $P < .05$.

RESULTS

The results of the measured dimensional accuracy of the width, length, and thickness are listed in (Table 2). The results of the conducted dimensional accuracy in the x,y coordinates (width and length) demonstrated that there was an insignificant lower mean of the width and length of the tested samples in all groups (3.992 ± 0.0109 mm, and 32.993 ± 0.0076 mm, respectively), compared to the CAD designs of the models in the same directions (4 mm, and 33 mm,

respectively). Results also showed that the mean of the measured dimensional accuracy in the z direction (thickness) of the tested samples in all groups (1.1366 ± 0.01417 mm) was significantly higher than that of the CAD designs (1 mm). Despite that, all groups, including the control printed samples, demonstrated a significant difference in the z direction compared to the virtual CAD designs. The results of the dimensional accuracy indicate that there were insignificant differences in the width, length, and thickness of the printed compact samples of the control group and the groups with hollow structures.

The mean and standard deviation of the weighting test of the samples shown in (Table 3), revealed a significantly lower weight of the samples of the Group 2, 3, and 4 at all volumetric reduction percentages compared to the control compact samples. The weighting test results also showed significant differences among the subgroups within each topologically modified group proportional to the volume reduction percentage. The weight of the samples was not dependent on the shape of the hollow geometries used in the Group 2, 3, and 4, where the weight of the samples was insignificantly different among the three groups at a

Table 2. The means and standard deviation of the dimensional accuracy of the samples in the x, y, and z directions

Subgroups	N	Reduction percentage %	Dimension means mm $\pm$ SD		
			Width (x)	Length (y)	Thickness (z)
CAD design	5	--	4.0000 $\pm$ .0000[a]	33.0000 $\pm$ .00000[b]	1.0000 $\pm$ .00000[c]
Compact	5	--	3.9960 $\pm$ .01673[a]	32.9920 $\pm$ .00837[b]	1.1300 $\pm$ .01000[d]
Spherical-based	5	10	3.9980 $\pm$ .00837[a]	32.9940 $\pm$ .00894[b]	1.1360 $\pm$ .02074[d]
Spherical-based	5	15	3.9860 $\pm$ .01140[a]	32.9900 $\pm$ .01000[b]	1.1300 $\pm$ .01000[d]
Spherical-based	5	20	3.9980 $\pm$ .00837[a]	32.9940 $\pm$ .00548[b]	1.1360 $\pm$ .01140[d]
Spherical-based	5	25	3.9860 $\pm$ .01140[a]	32.9920 $\pm$ .00837[b]	1.1360 $\pm$ .01140[d]
Ellipse-based	5	10	3.9900 $\pm$ .01000[a]	32.9980 $\pm$ .00447[b]	1.1340 $\pm$ .02074[d]
Ellipse-based	5	15	3.9980 $\pm$ .00837[a]	32.9940 $\pm$ .00894[b]	1.1440 $\pm$ .01517[d]
Ellipse-based	5	20	3.9880 $\pm$ .01095[a]	32.9920 $\pm$ .00837[b]	1.1360 $\pm$ .02074[d]
Ellipse-based	5	25	3.9900 $\pm$ .01000[a]	32.9980 $\pm$ .00447[b]	1.1360 $\pm$ .01342[d]
Diamond-based	5	10	3.9920 $\pm$ .01483[a]	32.9940 $\pm$ .00894[b]	1.1480 $\pm$ .00837[d]
Diamond-based	5	15	3.9960 $\pm$ .00548[a]	32.9940 $\pm$ .00894[b]	1.1360 $\pm$ .01517[d]
Diamond-based	5	20	3.9880 $\pm$ .00837[a]	32.9920 $\pm$ .00837[b]	1.1340 $\pm$ .01140[d]
Diamond-based	5	25	3.9920 $\pm$ .01483[a]	32.9940 $\pm$ .00894[b]	1.1400 $\pm$ .01581[d]
Sig. at $P < .05$			0.086	0.87	0.00

Where SD is the standard deviation, the means labeled with different letters indicate significant differences within the same column.

**Table 3.** The means and standard deviation of the weight test results of the four groups

Subgroups	N	Reduction percentage %	Weight (grams) $\pm$ SD
Control	5	--	1.22940 $\pm$ .00328[a]
Spherical-based	5	10	1.10160 $\pm$ .00207[b]
Spherical-based	5	15	1.04460 $\pm$ .00114[c]
Spherical-based	5	20	0.98400 $\pm$ .00291[d]
Spherical-based	5	25	0.92038 $\pm$ .001105[e]
Ellipse-based	5	10	1.10100 $\pm$ .001732[b]
Ellipse-based	5	15	1.04400 $\pm$ .002449[c]
Ellipse-based	5	20	0.98380 $\pm$ .004025[d]
Ellipse-based	5	25	0.92100 $\pm$ .002000[e]
Diamond-based	5	10	1.10180 $\pm$ .001304[b]
Diamond-based	5	15	1.04260 $\pm$ .002510[c]
Diamond-based	5	20	0.98420 $\pm$ .002683[d]
Diamond-based	5	25	0.92000 $\pm$ .003240[e]
Sig. at $P < .05$			0.00

Where SD is the standard deviation, the means labeled with different letters indicate significant differences within the same column.

specific volume reduction percentage.

The statistical analysis of the means of the yield tensile strength is shown in Fig. 5A. The results demonstrated that the yield tensile strength (YTS) of the Group 2 at a reduction (10%) per volume (485.2376 $\pm$ 4.71083 MPa) was insignificantly higher than that of the control group (480.0202 $\pm$ 4.0896 MPa) and significantly higher than the rest of the subgroups. Indicating that the sphere-based hollow structure increased the yield strength of the samples integrated
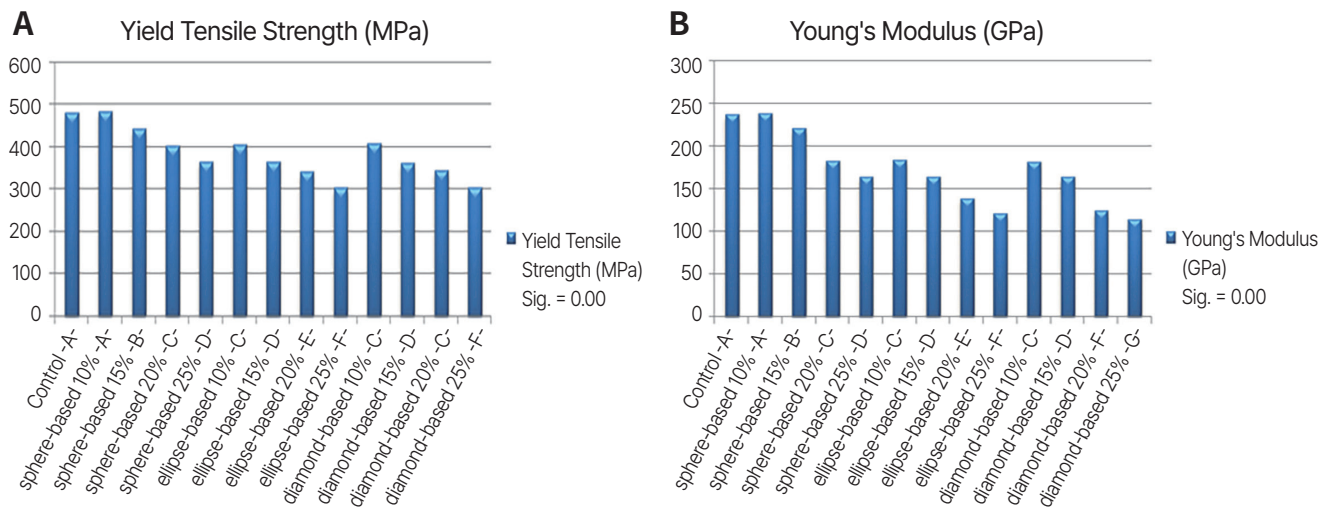
Fig. 5. Bar graphs of the means of (A) the yield tensile strength (B) Young's modulus. According to ANOVA and Duncan's multiple range tests at *P* < .05. Bar names with different letters indicate significant differences.

with the hollow structure to be equivalent to that of the compact samples at a 10% volume reduction. The results of the statistical analysis of the yield strength revealed a gradual decrease in the yield strength as the volumetric reduction percentage increased, where the YTS of the samples in the Group 2 was significantly different among the four subgroups at (10%, 15%, 20%, and 25%) volume reduction. The statistical comparison among the groups showed that the YTS of the Group 2 at 10% and 15% volume reduction was significantly higher than the subgroups of the Group 3 and 4. Indicating that the YTS of the samples integrated with hollow structures depended on the shape of the hollow structure used. The results demonstrated that the YTS means of Group 3 and 4 were significantly lower than that of Group 2 with the same volumetric reductions; however, the YTS of Group 3 and 4 had the same pattern of strength reduction as that of the Group 2 where the YTS values were inversely proportional to the volumetric reduction percentages.

The results of the elastic modulus (E) analysis showed a declination according to the geometry used and the reduction of volume as illustrated in Fig. 5B. The mean of the E in Group 2 at a 10% reduction percentage per volume (239.3188 $\pm$ 4.4838 GPa) was insignificantly higher than that of the control group (237.1862 $\pm$ 5.2432 GPa), indicating comparable

means of the Young's modulus between the control group and the Group 2 at a 10% volume reduction. The statistical evaluation of the E showed a gradual decrease in the E values in Group 2 that was inversely proportional to the volumetric reduction percentage and proportional to the reduction of the YTS values. The results of the E in Group 3 and 4 followed the same regression pattern as that in Group 2, which was directly proportional to the YTS and inversely proportional to the volumetric reduction. The statistical analysis of the E among the groups demonstrated that the E values of Group 2 were significantly higher than that of the Group 3 and 4 when the volume reduction percentage was equal.

The microscopic inspection of the cross sections at the sample's body other than the fracture area shown in Fig. 6 (A, B, C) illustrated a valid reproduction of the hollow geometries of the Group 2, 3, and 4, where the sphere-based and the ellipse-based geometries were perfectly outlined in the cross sections. In contrast, the diamond-based geometry had less accuracy with an acceptable rhomboidal outline. The microscopic inspection of the fractographs shown in Fig. 6 (D, E, F, G) illustrated that the hollow basic geometries were slightly changed due to the tensional stress. The crack propagation in the fractographs was noticed in Group 1 near the lateral end of the sample as a non-split

unidirectional crack. In Group 2 with sphere-based geometry, the crack was split with an arc shape, located within the metallic shell of the hollow sphere structure, and its direction was perpendicular to the direction of the applied stress. In contrast, the crack propagation was not clear in the ellipse-based and diamond-based geometriesprobably because the crack did not split or was not redirected by the geometrical shapes and ran within the fracture lines.

DISCUSSION

In the current paper, the internally architected hollow structures were sphere-based, ellipse-based, and diamond-based geometries representing three principal physical shapes: the arc, straight line, and sharp angle, respectively. The validity of the printing of the internally designed hollow structures was evaluated by non-destructive testing using digital X-ray, the dimensional accuracy of the printed objects was measured, and the yield tensile strength and Young's modulus were calibrated to find the role of the designed hollow structures on the dimensional accuracy and the mechanical performance of the samples.

Results have shown that the dimensional accuracy of the 3D printed models was insignificantly lower
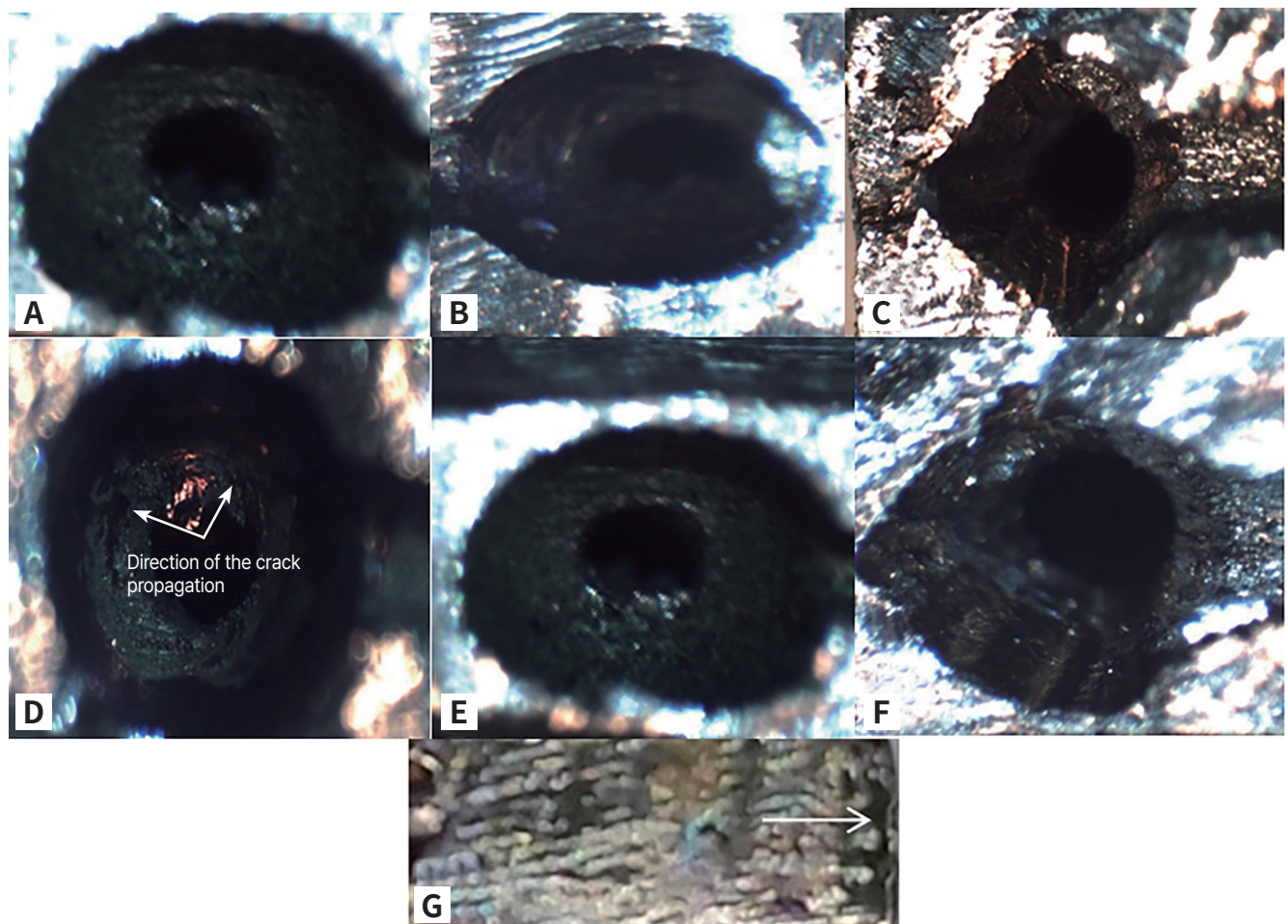
Fig. 6. Microscopic images of samples' cross sections (A, B, C) Microscopic images of cut cross sections of the sphere, ellipse, and diamond-based geometries, respectively. (D) Fractograph of the sphere-based geometry with multiple cracks formation (white arrows). (E) Fractograph of the ellipse-based geometry showing hollow shape changes due to the induced tension. (F) Fractograph of the diamond-based geometry showing hollow shape changes due to the induced tension. (G) Fractograph of the sphere-based geometry with crack formation (white arrows).

than that of the CAD values in the width and length, but the dimensional measurements of the samples' thickness were significantly higher than the CAD designs in all groups, including the control samples; these results showed that there were insignificant differences in the three dimensions (x, y, z) among the compact samples and the other groups with incorporated hollow geometries at all levels of volume reduction, and shapes of the basic hollow geometry. Also, the sphere-based hollow structures with a 10% reduction percentage per volume had insignificantly higher means of the yield tensile strength when compared to the compact samples and significantly higher mean of the yield tensile strength compared to the other types of geometries in Group 3 and 4. This indicates that the sphere-based hollow structure at a 10% volume reduction was able to produce weight reduced samples with a tensile strength that is equivalent to the compact samples and higher than other types of the geometries without producing significant changes in the elastic modulus and dimensional accuracy of the printing compared to the compact samples. According to these results, the study hypothesis was accepted.

The results revealed a significantly lower means of the z coordinate (thickness) of the CAD designed samples compared to the printed samples, including the control group in the buildup direction, probably because of the inaccuracy of the descending piston on the level of millimeter fraction. The slight reduction of x,y measurements could be the resulting layout of the samples (transversally at 0°) during the printing process without using supporting structures where the first layer positioned directly at the printing table led to slight shrinkage due to the residual heat stresses generated by the laser beam.[26,27] The dimensional accuracy test of the groups indicated that the dimensional accuracy was independent of the geometry of the integrated hollow structures. Still, more logically, it depended on the software programs in the CAD-CAM process. The AM building process is competent with the tessellation and machine accuracy. The Magics slicing program creates denser and more precise meshes than comparable CAD products; a more precise algorithm limits triangle bordering lengths. This method allows for a less uneven finishing when printing metallic objects, which improves the transmission of design information to the printing machine and results in more precise printings when compared to the initially generated CAD files.[28] Also, the use of the laser-powder bed fusion (L-PBF) in the fabrication of the metallic denture bases reduced the total discrepancies of frames, where the fabricated frameworks had significantly higher precision than those of traditionally manufactured structures, indicating higher accuracy of the 3D printed objects.[28,29] The current study supports the previous study's findings that no appreciable differences exist between the additively built parts and CAD designs in the x and y directions and that significantly higher difference exists in z direction measurements.[27]

The results revealed a significant reduction in weighted samples compared to the compact samples. Also, the weights of the tested samples were significantly different at different reduction percentages. The internally integrated hollow structures can decrease the mass of the additively manufactured objects due to the apparent reduction in density, consequently reducing the cost and period of the printing procedure.[30,31] These results are consistent with previous studies that confirmed a significant mass reduction when hollow structures are incorporated inside the printed object relative to the reduction in density of the item.[32,33]

The yield tensile strength test was conducted to evaluate the tensile strength and Young's elastic modulus of the as-built printed Co-Cr specimens using the DMLS technique. The yield tensile strength and the modulus of elasticity were calculated depending on the 0.2% strain offset at the stress/strain curve. The yield tensile strength was evaluated due to its high importance of revealing the strength point within the elastic limit, where no plastic deformation occurs in the object, which is undesirable deformation in the dental restoration which, consequently, will produce irreversible deformation in the dimensional accuracy and fitness of the removable partial denture. The results revealed an insignificant higher mean of the yield strength in the sphere-based hollow structure at 10% volume reduction compared to the compact control group and a significantly higher mean of the yield strength compared to other topologic modifications

with graded densities, indicating that the incorporation of the sphere-based hollow structure improved the tension properties of the density reduced objects at a specific reduction of volume (10%). There was a significantly lower mean of the yield strength of the sphere-based hollow samples at 15% reduction percentage compared to the compact and sphere-based samples of 10% volume reduction, which pointed to the start of the yield tensile strength declination due to more reduction of the density of the printed items. Results also showed insignificant differences among the means of Young's modulus at this volumetric reduction (10%) compared to the control group, which indicates that the material's stiffness has not changed due to the sphere-based internal geometries integrated into the samples at a 10% reduction per volume. The decrease in the resistance of the objects to the tension force was observed as the reduction percentage increased and when varied shapes of interior geometries were utilized. The findings provided in this study illustrate that the incorporation of engineered sphere-based voids has significant promise for enhancing the structural integrity of components and frameworks produced by the DMLS method that contain hollow structures to reduce weight. The observed enhancement in fracture resistance accompanied the obvious weight reduction corresponding to the volumetric reduction percentage used in this study. The yield strength of the samples incorporated with sphere-based hollow structures at 10% volume reduction was significantly higher than those of other geometry shapes, specifically attributed to a geometric alteration. This alteration could be the result of the internal gaseous pressure induced in the spherical void inside the solid structures that could enhance the stress resistance; the effect of the algorithmic rise in the gaseous pressure inside the confined geometries could be more applicable in situations when compression forces were applied.[22] It may also be attributed to the arrest and termination of cracks. The crack propagation could be reoriented in a direction parallel to the applied force instead of a perpendicular one, in the presence of angle-free arc surfaces micro-voids like the spherical geometry that can reduce the stress concentration on a specific point, leading to resolution of the applied forces in more than one direction; this effect was amplified by the presence of the horizontal cylindrical connectors that redirected the crack propagation to a direction perpendicular to original crack propagation vector, leading to a better strength quality of the object.[34,35] In addition, the crack propagation intensity could be split and bifurcated by the presence of angle-free micro-voids inside the solid body; the splitting and bifurcation of the crack intensity are evident in the sphere-based geometry due to the sphere-shaped shell of metal that surrounds the void. This effect is absent in the geometry with sharp angles represented by the diamond-based hollow structure, and the straight lines represented by the dorsum of the hollow ellipse that was located transversally.[36] The effect of the hollow structures can also be clarified by the fact that the objects incorporated with internal hollow structures can absorb a higher amount of the energy induced by the externally applied stress.[8,9,37,38] In contrast, conventional geometries experienced catastrophic fractures at very low driving pressures. The results showed a reduction in the tensile strength with different hollow shapes, and the increase in the volume reduction can be explained by the fact that different geometries with graded density within the object can induce different levels of energy absorption and different interaction with the crack terminal. In addition, the larger voids with the lower density of these voids can play as a focal point for the crack propagation.[36,37,39-41]

The results revealed a significantly higher means of Young's modulus in the control group and Group 2 at a 10% volume reduction than the rest of the subgroups. The Young's modulus means showed a gradual regression relative to the yield strength declination and increased reduction percentage in each subgroup, where it was the highest in the sphere-based structure at 10% volume reduction followed by insignificantly lower mean of the control group. The lowest mean of elastic modulus was in the ellipse-based and diamond-based geometries at 25% volume reduction. The gradual reduction of the mean of the elastic modulus was clearly affected by the gradual reduction of the yield tensile strength when the strain of the measured objects was nearly the same. This phenomenon is usually accompanied by high brittleness and extremely lower flexibility because of the

less grain dislocation of the samples that were tested as built without heat treatment; in addition, the samples were printed transversally in a perpendicular direction to the applied force during testing, which also contributed to less grain dislocation of the untreated printed samples.[42-44]

The accuracy of the hollow-shaped topological manufacturing can be assessed through radiographic evaluation or microscopic study of the fractographs.[45,46] The study investigated the microscopic images of the produced model obtained from the topology-modified geometrical architecture constructed with direct selective laser sintering (DMLS). The analysis was performed utilizing a visual qualitative inspection. The cross-sectional area analyses of the printed hollow shapes demonstrated that the DMLS process effectively produced all shapes. Furthermore, the examination of the cross sections of the three geometries revealed that the geometric shapes with circular forms in the sphere and ellipse were printed satisfactorily, with no or minimal residual defects. On the other hand, the diamond-shaped objects showed more significant variations, particularly in the upper and lower regions near the sharp angles in the printing direction; this suggests that hollow shapes with sharp angles may have lower printing quality than angle-free circular shapes. These findings suggest that the parameters employed in the DMLS procedure and the selected relocation position were suitable for the production of the hollow structures.[47-49] The crack propagation present in the sphere-based geometry supported the idea that the crack split was redirected by the metallic shell surrounding the sphere shapes due to the absence of straight lines and angles in the designed sphere pattern.[36]

The main limitation of the current study was that the proposed geometries were not optimized to the exact reduction percentage using the artificial intelligence programs, or FEA, so it can be suggested that one of the software analysis programs be used to study the proposed geometries. The proposed hollow structures were not tested in clinical situations, especially after aging in the oral environment; for this reason, further studies are recommended to be conducted in clinically simulated circumstances.

CONCLUSION

In the current study, three types of internal geometries were used to design three different hollow structures incorporated in the core of the dog-bone tensile specimen with a graded reduction of the specimen volume (10%, 15%, 20%, and 25%). Results of the yield strength revealed that the sphere-based hollow structure at 10% volume reduction was superior to the other types of geometries and can be considered as a novel internal topologic design that can achieve equivalent yield tensile strength comparable to the compact designs. In contrast, the diamond-based and ellipse-based geometries of 25% volume reduction had the lowest means of strength relative to the volumetric reduction. Results also demonstrated that the graded increase in reduction of volume resulted in a gradual decrease in the strength and the modulus of elasticity for all geometries. The dimensional accuracy exhibited insignificantly lower means of the measured x, y, z coordinates of the test groups compared to the compact control group, suggesting that the printing accuracy was not correlated to the geometries' presence, size, or type. The weighing test results revealed significant differences among the test groups and the control groups at 10%, 15%, 20%, and 25% volume reduction.

REFERENCES

1. Steuben JC, Iliopoulos AP, Michopoulos JG. Towards multiscale topology optimization for additively manufactured components using implicit slicing. In: International design engineering technical conferences and computers and information in engineering conference. American Soc Mech Engi 2017:V001T02A024.

2. Khorsandi D, Fahimipour A, Abasian P, Saber SS, Seyedi M, Ghanavati S, Ahmad A, De Stephanis AA, Taghavinezhaddilami F, Leonova A, Mohammadinejad R, Shabani M, Mazzolai B, Mattoli V, Tay FR, Makvandi P. 3D and 4D printing in dentistry and maxillofacial surgery: Printing techniques, materials, and applications. Acta Biomater 2021;122:26-49.

3. Kränzlin N, Niederberger M. Controlled fabrication of porous metals from the nanometer to the macroscopic scale. Mater Horiz 2015;4:359-77.

4. Plocher J, Panesar A. Review on design and structural optimisation in additive manufacturing: Towards next-generation lightweight structures. Mater Des 2019;183:108164.

5. Babamiri B, Barnes B, Soltani-Tehrani A, Shamsaei N, Hazeli K. Designing additively manufactured lattice structures based on deformation mechanisms. Addit Manuf 2021;46:102143.

6. Zhu JH, Zhang WH, Xia L. Topology optimization in aircraft and aerospace structures design. Arch Comput Methods Eng 2016;23:595-622.

7. Kladovasilakis N, Tsongas K, Karalekas D, Tzetzis D. Architected materials for additive manufacturing: a comprehensive review. Materials 2022;15:5919.

8. Abueidda DW, Bakir M, Al-Rub RKA, Bergström JS, Sobh NA, Jasiuk I. Mechanical properties of 3D printed polymeric cellular materials with triply periodic minimal surface architectures. Mater Des 2017;122:255-67.

9. Al-Saedi DSJ, Masood SH, Faizan-Ur-Rab M, Alomarah A, Ponnusamy P. Mechanical properties and energy absorption capability of functionally graded F2BCC lattice fabricated by SLM. Mater Des 2018;144:32-44.

10. Xiao Z, Yang Y, Xiao R, Bai Y, Song C, Wang D. Evaluation of topology-optimized lattice structures manufactured via selective laser melting. Mater Des 2018;143:27-37.

11. Gu DD, Meiners W, Wissenbach K, Poprawe R. Laser additive manufacturing of metallic components: materials, processes and mechanisms. Int Mater Rev 2012;57:133-64.

12. Paper R. Investigation of metallic 3D porous scaffold prepared by selective laser sintering for dental applications. Nanochem Res 2023;8:122-33.

13. Goh GD, Sing SL, Yeong WY. A review on machine learning in 3D printing: applications, potential, and challenges. Artificial Intelligence Rev 2021;54:63-94.

14. Koutsoukis T, Zinelis S, Eliades G, Al-Wazzan K, Rifaiy MA, Al Jabbari YS. Selective laser melting technique of Co-Cr dental alloys: a review of structure and properties and comparative analysis with other available techniques. J Prosthodont 2015;24:303-12.

15. Huang R, Ulu E, Kara LB, Whitefoot KS. Cost minimization in metal additive manufacturing using concurrent structure and process optimization. In: International design engineering technical conferences and computers and information in engineering conference. American Soc Mech Eng 2017. p. V02AT03A030.

16. Galeta T, Raos P, Stoj i J, Pak i I. Influence of structure on mechanical properties of 3D printed objects. Procedia Eng 2016;149:100-4.

17. Challis VJ, Roberts AP, Wilkins AH. Design of three dimensional isotropic microstructures for maximized stiffness and conductivity. Int J Solids Struct 2008;45:4130-46.

18. Lesueur M, Poulet T, Veveakis M. Predicting the yield strength of a 3D printed porous material from its internal geometry. Addit Manuf 2021;44:102061.

19. ISO 22674. Metallic materials for fixed and removable restorations and appliances. International Standards Organization (ISO); Geneva; Switzerland, 2016.

20. ASTM Committee E28. ASTM E9-89a. Stand test methods compression test met mater room temp. 2000; (Reapproved):1-9.

21. Xiong Y, Yao S, Zhao ZL, Xie YM. A new approach to eliminating enclosed voids in topology optimization for additive manufacturing. Addit Manuf 2020;32:101006.

22. MacKenzie JK. The elastic constants of a solid containing spherical holes. Proc Phys Soc Sect B 1950;63:2-11.

23. Sas W, Gluchowski A, Szymanski A. Impact of the stabilization of compacted cohesive soil-sandy clayon yield criterion improvement. Ann Warsaw Univ Life Sci L Reclam 2014;46:139-51.

24. Smith I, Foliente GC. Load and resistance factor design of timber joints: International practice and future direction. J Struct Eng 2002;128:48-59.

25. Zupancic R, Legat A, Funduk N. Tensile strength and corrosion resistance of brazed and laser-welded cobalt-chromium alloy joints. J Prosthet Dent 2006;96:273-82.

26. Unkovskiy A, Bui PH, Schille C, Geis-Gerstorfer J, Huettig F, Spintzyk S. Objects build orientation, positioning, and curing influence dimensional accuracy and flexural properties of stereolithographically printed resin. Dent Mater 2018;34:e324-33.

27. Islam MN, Boswell B, Pramanik A. An investigation of dimensional accuracy of parts produced by three-dimensional printing. In: Proceedings of the World Congress on Engineering 2013. IAENG; 2013. p. 522-5.

28. Hällgren S, Pejryd L, Ekengren J. 3D data export for additive manufacturing-improving geometric accuracy. Procedia Cirp 2016;50:518-23.

29. Peng PW, Hsu CY, Huang HY, Chao JC, Lee WF. Trueness of removable partial denture frameworks additively manufactured with selective laser melting. J Prosthet Dent 2022;127:122-7.

30. Okano H, Tasaka A, Matsunaga S, Kasahara M, Wadachi J, Hattori M, Abe S, Yamashita S. Effects of hollow structures added by selective laser sintering on the mechanical properties of Co-Cr alloy. J Prosthodont Res 2023;67:460-7.

31. Kocak EF, Ekren O, Ucar Y. Effect of internal design modification on the mechanical properties of laser sintered cobalt-chromium multi-unit metal-ceramic frameworks. J Prosthodont 2022;31:766-70.

32. Chiu LNS, Rolfe B, Wu X, Yan W. Effect of stiffness anisotropy on topology optimisation of additively manufactured structures. Eng Struct 2018;171:842-8.

33. Orme ME, Gschweitl M, Ferrari M, Madera I, Mouriaux F. Designing for additive manufacturing: Lightweighting through topology optimization enables lunar spacecraft. J Mech Des Trans ASME 2017;139:100905-6.

34. Conway K, Kunka C, White BC, Pataky GJ, Boyce BL. Increasing fracture toughness via architected porosity. Mater Des 2021;205:109696.

35. Al-Ketan O, Rowshan R, Palazotto AN, Abu Al-Rub RK. On mechanical properties of cellular steel solids with shell-like periodic architectures fabricated by selective laser sintering. J Eng Mater Technol Trans ASME 2019;141:021009.

36. Liu YJ, Ren DC, Li SJ, Wang H, Zhang LC, Sercombe TB. Enhanced fatigue characteristics of a topology-optimized porous titanium structure produced by selective laser melting. Addit Manuf 2020;32:101060.

37. Challis VJ, Xu X, Zhang LC, Roberts AP, Grotowski JF, Sercombe TB. High specific strength and stiffness structures produced using selective laser melting. Mater Des 2014;63:783-8.

38. Takezawa A, Koizumi Y, Kobashi M. High-stiffness and strength porous maraging steel via topology optimization and selective laser melting. Addit Manuf 2017; 18:194-202.

39. Yoder S, Morgan S, Kinzy C, Barnes E, Kirka M, Paquit V, Nandwana P, Plotkowski A, Dehoff RR, Babu SS. Characterization of topology optimized Ti-6Al-4V components using electron beam powder bed fusion. Addit Manuf 2018;19:184-96.

40. Al-Ketan O, Rowshan R, Al-Rub RKA. Topology-mechanical property relationship of 3D printed strut, skeletal, and sheet based periodic metallic cellular materials. Addit Manuf 2018;19:167-83.

41. Ferro P, Meneghello R, Razavi SMJ, Berto F, Savio G. Porosity inducing process parameters in selective laser melted AlSi10Mg aluminium alloy. Phys Mesomech 2020;23:256-62.

42. Geiger F, Kunze K, Etter T. Tailoring the texture of IN-738LC processed by selective laser melting (SLM) by specific scanning strategies. Mater Sci Eng A 2016;661: 240-6.

43. Pellizzari M, Jam A, Tschon M, Fini M, Lora C, Benedetti M. A 3D-printed ultra-low young's modulus β-Ti alloy for biomedical applications. Materials 2020;13:2792.

44. Etter T, Kunze K, Geiger F, Meidani H. Reduction in mechanical anisotropy through high temperature heat treatment of Hastelloy X processed by Selective Laser Melting (SLM). In: IOP Conference Series: Materials Science and Engineering. IOP Publishing; 2015. p. 12097.

45. Astuti ER, Arifin AZ, Indraswari R, Putra RH, Ramadhani NF, Pramatika B. Computer-aided system of the mandibular cortical bone porosity assessment on digital panoramic radiographs. Eur J Dent 2023;17:464-71.

46. Putri TS, Hayashi K, Ishikawa K. Fabrication of three-dimensional interconnected porous blocks composed of robust carbonate apatite frameworks. Ceram Int 2020;46:20045-9.

47. Song J, Wang Y, Zhou W, Fan R, Yu B, Lu Y, Li L. Topology optimization-guided lattice composites and their mechanical characterizations. Compos Part B Eng 2019;160:402-11.

48. Maconachie T, Leary M, Lozanovski B, Zhang X, Qian M, Faruque O, Brandt M. SLM lattice structures: Properties, performance, applications and challenges. Mater Des 2019;183:108137.

49. Vilardell AM, Takezawa A, Du Plessis A, Takata N, Krakhmalev P, Kobashi M, Yadroitsava I, Yadroitsev I. Topology optimization and characterization of Ti6Al4V ELI cellular lattice structures by laser powder bed fusion for biomedical applications. Mater Sci Eng A 2019;766:138330.